Journal of Solid State Chemistry 270 (2019) 470–478

Contents lists available at ScienceDirect

Journal of Solid State Chemistry

journal homepage: www.elsevier.com/locate/jssc

Structural and thermodynamic mixing properties of $La_{1-x}Nd_xPO_4$ monazite-type solid solutions

H. Schlenz[a,*,1], J. Dellen[a,2], P. Kegler[a], C. Gatzen[a,1], C. Schreinemachers[a], A. Shelyug[b], M. Klinkenberg[a], A. Navrotsky[b], D. Bosbach[a]

[a] Forschungszentrum Jülich GmbH, Institute of Energy and Climate Research (IEK), IEK-6: Nuclear Waste Management and Reactor Safety, D-52425 Jülich, Germany

[b] Peter A. Rock Thermochemistry Laboratory and NEAT ORU, University of California Davis, Davis, CA 95616, USA

ARTICLE INFO

Keywords:
Monazite
Solid solution
Crystal structure
Nuclear waste
Actinides
Enthalpy of mixing

ABSTRACT

$La_{1-x}Nd_xPO_4$ monazite-type ceramics were synthesized by precipitation and sintering. The obtained crystalline powders and pellets were structurally characterized by X-ray diffraction, electron microscopy, and infrared and Raman spectroscopy. The determined unit cell constants agree with published values for the pure end-members ranging from $LaPO_4$ to $DyPO_4$, as well as with values for known mixed monazite-type lanthanide orthophosphates, indicating a homogeneous solid solution. However, Raman spectroscopy shows a change in short-range order and the results of high temperature oxide melt solution calorimetry suggest a subregular solid solution, which requires two Margules parameters to calculate the observed enthalpy of mixing ΔH_{mix} for $La_{1-x}Nd_xPO_4$, which is positive and asymmetric and shows a maximum at x = 0.299 (ΔH_{mix} = 7.53 ± 0.01kJ mol^{-1}) at 298 K.

1. Introduction

Monazite-type solid solutions with general composition $LnPO_4$ (*Ln*=La to Gd) are considered as ceramic immobilization matrices for the conditioning of actinides like U, Np, Pu, Am and Cm [1–5]. Monazite-type binary solid solutions represent suitable model systems for the investigation of characteristic properties of mixed orthophosphates. The chemical composition of the mineral monazite is dominated by several lanthanides as well as actinides like thorium and uranium. The crystal structure remains intact over very long time periods despite the ongoing radiation exposure. Such ceramic phases can contain one, two or even more cations on the variable *Ln* position. Although it has long been known that monazite shows outstanding radiation resistance and chemical durability [6], even a rather simple system like $La_{1-x}Nd_xPO_4$, where Nd^{3+} is a possible surrogate for Am^{3+}, is not yet fully understood in terms of structure and stability. The aim of the present study is to investigate the crystal structure and thermodynamic properties of $LaPO_4$ – $NdPO_4$ solid solutions and to understand the microscopic (structural) reasons for the observed thermodynamic behaviour.

Recent publications differ regarding the structural character of $La_{1-x}Nd_xPO_4$ solid solutions. Palke and Stebbins [7], who performed ^{31}P nuclear magnetic resonance (NMR) experiments on this system, stated that $La_{1-x}Nd_xPO_4$ is not a single phase, but is more likely a phase with $LaPO_4$-rich chemical inhomogeneities, where the dissolution of $NdPO_4$ into $LaPO_4$ is not complete. On the other hand, Maron et al. [8], who also performed ^{31}P NMR and additionally electron spin resonance (ESR) experiments, concluded that $La_{1-x}Nd_xPO_4$ actually is a single phase, and they emphasized the importance of synthesis and preparation procedures. The clarification of this contradiction represents the first part of our motivation to investigate this particular system.

There are few prior thermodynamic studies of solid solutions in this system. Popa et al. [9] determined the excess enthalpy between 515 K and 1565 K. This is an excess heat content reflecting differences in heat capacities and not a heat of mixing and will not be discussed further. Li et al. [10] performed DFT calculations to obtain heats of mixing in the solid solution. The values were positive (endothermic) and were fit to a subregular mixing model. Get'man and Radio [35], calculated the mixing energies of some monazite-type solid solutions, based on the assumption of a symmetric regular solution, with no significant change in short-range ordering, and therefore consequently only one Margules interaction parameter was considered. To the best of our knowledge there are no direct calorimetric determinations of heats of mixing in this system, so obtaining such values on well characterized samples

* Corresponding author.
E-mail address: h.schlenz@fz-juelich.de (H. Schlenz).
[1] Present address: Forschungszentrum Jülich GmbH, IEK-1: Materials Synthesis and Processing, D-52425 Jülich, Germany.
[2] Present address: RWTH Aachen, Institut für Gesteinshüttenkunde, Mauerstr. 5, D-52064 Aachen, Germany.

https://doi.org/10.1016/j.jssc.2018.11.040
Received 9 October 2018; Received in revised form 27 November 2018; Accepted 29 November 2018
Available online 03 December 2018
0022-4596/ © 2018 Elsevier Inc. All rights reserved.

using high temperature oxide melt solution calorimetry is a major goal of the present study. To this end, we have synthesized 20 different compositions of $La_{1-x}Nd_xPO_4$, and investigated their homogeneity and crystal structure using powder X-ray diffraction, electron microscopy (SEM for elemental analysis using energy-dispersive X-ray spectrometry; see Section 2.2), and infrared and Raman spectroscopy. The mixing properties were determined by high temperature oxide melt solution calorimetry. Our goal is to obtain a comprehensive picture of this system and to relate the thermodynamic mixing properties to possible short range order and structural evolution in the solid solution.

2. Experimental methods

2.1. Synthesis

All compounds were synthesized by precipitation reactions out of aqueous solutions. Therefore the following easily soluble salts were used: $Nd(NO_3)_3{\cdot}H_2O$ (≥ 99.9%, Ventron GmbH), $La(NO_3)_3{\cdot}6\,H_2O$ (≥ 99.9%, Aldrich), and $(NH_4)_2HPO_4$ (≥ 99.0%, Merck). The appropiate masses of $La(NO_3){\cdot}6\,H_2O$ were weighed in glass crucibles and diluted with distilled water. Then volumes of the $Nd(NO_3)_3$-solution were filled into the same crucibles. The needed amounts of $(NH_4)_2HPO_4$ were diluted in 20 mL vials with distilled water. Finally all solutions were mixed under continuous stirring. Slowly a rosy precipitate was formed which then was dried at 363 K, followed by heat treatment of the samples for ten hours at 1073 K and atmospheric pressure. Through this step remaining NO_x was evolved. The obtained samples were well ground in an corundum mortar and then five pellets of 1 g and 10 mm diameter each were pressed for all compositions. The pellets were finally sintered at 1723 K on a platinum sheet for eight hours, different to the work of Popa et al [9] who treated their samples at 1373 K without sintering.

2.2. Analytical methods

After synthesis the samples were chemically investigated by scanning electron microscopy (SEM) using a Quanta 200F (*FEI*) equipped with a Genesis EDAX-system. Using energy dispersive X-ray spectroscopy (EDX) in a vacuum of 60 Pa operating at 20 kV, the ratio $\frac{(La,Nd)}{P}$ was determined to 1.002 ± 0.020 and therefore very close to the optimum value 1.0. No other elements could be detected than La, Nd, and P (O was calculated). The determined mole fractions of La for the samples under investigation are given in Tables 1 and 2 and in the tables in the supplementary information, with an estimated average uncertainty of ± 0.004.

A *Bruker* D4 Endeavor diffractometer with Cu $K_{\bar{\alpha}}$ (λ = 1.54187 Å) was used for powder X-ray diffraction (XRD) measurements, equipped with an one-dimensional silicon strip LynxEye detector (*Bruker*), using a voltage of 40 kV and an electric current of 40 mA (1.6 kW). Data were recorded in the range $2\Theta = 10 - 130°$ (total counting time=10 s/step; stepsize=0.01° 2Θ; 5 separate runs with 2 s/step each). The aperture of the fixed divergence slit was set to 0.2 mm and the aperture of the receiving slit to 8.0 mm. In order to reduce possible fluorescence effects, the discriminator of the detector was set to an interval of 0.16–0.25 V. Complete Rietveld refinements were performed using the software TOPAS 4.2 (*Bruker*), which enables the application of fundamental parameters for the definition of peak shape functions, using e.g. the precise diffractometer geometry.

Unpolarized Raman spectra were recorded using a *Horiba* LabRAM HR spectrometer equipped with a Peltier cooled multi-channel CCD detector. An objective with 50x magnification was linked to the spectrometer allowing the analysis of samples as small as 2 µm in diameter (sintered pellets). The incident radiation was produced by a HeNe laser at a power of 17 mW (λ_0 = 632.81 nm). The focal length of the spectrometer was 800 mm and a 1800 gr/mm grating was used. The spectral resolution was around 1 cm^{-1} with a slit of 100 µm. Spectra were recorded in the range 100 – 1250 cm^{-1}. No significant photoluminescence (PL) was observed.

Infrared spectroscopic investigations were carried out in the wavenumber range of 400 – 4000 cm^{-1} using a *Bruker* AXS FT-IR spectrometer EQUINOX 55. Approximately 1 mg of the as prepared as well as the sintered powder of each sample was mixed with 250 mg KBr and pressed to pellets for the measurements. Opus software (*Bruker*) was used for peak search.

2.3. Calorimetric measurements

High temperature oxide melt solution calorimetry allows the determination of the enthalpy of formation ΔH°_f of a chemical compound directly from the heat effect caused by a sample that is dropped into a molten solvent of constant temperature [11]. The measured heat effect (enthalpy of drop solution, ΔH_{ds}) is a sum of two effects: the heating of the sample from room temperature to the temperature of the solvent (usually 973 K or 1073 K) and the enthalpy of dissolution of the sample in the solvent, which may include effects from oxidation state change or gas evolution. High temperature drop solution calorimetry of this work was performed using a custom build Tian-Calvet-type twin calorimeter at 973 K [12,13]. The calorimeter was calibrated by measuring the heat content of $\alpha - Al_2O_3$ pellets. Each side of the twin calorimeter contained a Pt-crucible with 20 g of sodium molybdate solvent ($3\,Na_2O{\cdot}4\,MoO_3$). For each measurement, approximately 5 mg of the sample were pressed to a cylindrical pellet of 1 mm diameter, accurately weighed on a microbalance, and then dropped into the solvent. All samples were thermally treated at 1073 K for at least 8 h prior the calorimetric measurements, in order to remove possible adhesive water from the surface. At least 8–10 drops were performed per composition. To prevent slow dissolution or saturation of the solvent not more than 60 mg of sample was dropped into one batch of 20 g solvent. During the measurement the melt was stirred by bubbling with oxygen (flow rate 5.9 mL/min). This assures an oxidative environment and also enhances the dissolution and prevents a local saturation of the solvent [11]. In addition, a constant flow of O_2 gas was flushed through the calorimeter chamber (40 mL/min) to generate a constant gas environment above the solvent and to remove any evolved created gases. The integral of the heat flow versus time curve for the duration of the experiment, after applying the appropriate calibration factor, provided the measured heat effect. Only reactions that returned to the initial baseline signal within an hour were used. The methodology has been described in numerous papers and applied extensively to rare earth oxide materials (see e.g. [11] and references therein). The measured signal of heat flow over time was integrated using the software CALISTO (Setaram) to calculate ΔH_{ds}. The achievable accuracy of ΔH_{ds} is about ±1 kJ mol^{-1} (see Tables 1 and 2). Using appropriate thermochemical cycles, enthalpies of formation from oxides and elements as well as the enthalpy of mixing were calculated (Table 2). Table 1 shows an example of a thermochemical cycle for the calculation of the enthalpy of formation from oxides and elements at 298 K for $La_{1-x}Nd_xPO_4$ from drop solution experiments. In order to determine the enthalpy of mixing the values of the enthalpy of drop solution were subtracted from a composition weighted average of the enthalpy of drop solution of the two end members.

3. Results and discussion

3.1. X-ray powder diffraction and Rietveld refinements

Only Bragg reflections that refer to monazite (space group $P\,2_1/n$) were observed and all samples appeared to be single phases. With increasing Nd content we observed a continuous shift of all Bragg reflections to higher diffraction angles. Fig. 1 shows the shift of the (120) reflection from 28.7° to 29.1° from pure $LaPO_4$ to pure $NdPO_4$,

Table 1
Thermochemical cycle for the determination of the enthalpy of formation of $La_{1-x}Nd_xPO_4$ solid solutions from oxides and elements. The subscripts correspond to: s = solid, 298 = 298 K, 973 = 973 K, sln=solution, ds=drop solution, cr=crystalline, g=gaseous. [a] from [42]. [b] from [14]. [c] from [43]. [d] from [44]. The errors of ΔH are two standard deviations of the mean for the as measured values and are propagated for the calculated values.

Reaction		ΔH(kJ mol^{-1})
$(La_{1-x}Nd_x)PO_{4(s,298)} \rightarrow \frac{1}{2}(1-x)La_2O_{3(sln,973)} + \frac{1}{2}xNd_2O_{3(sln,973)} + \frac{1}{2}P_2O_{5(sln,973)}$	(1) ΔH_{ds} $(La_{1-x}Nd_x)PO_4$	see Table 2
$La_2O_{3(cr,298)} \rightarrow La_2O_{3(sln,973)}$	(2) ΔH_{ds} La_2O_3	−225.10 ± 3. 16[a]
$Nd_2O_{3(cr,298)} \rightarrow Nd_2O_{3(sln,973)}$	(3) ΔH_{ds} Nd_2O_3	−163.40 ± 3. 44[b]
$P_2O_{5(cr,298)} \rightarrow P_2O_{5(sln,973)}$	(4) ΔH_{ds} P_2O_5	−164.6 ± 0. 5[b]
$2Nd_{(s,298)} + \frac{3}{2}O_{2(g,298)} \rightarrow Nd_2O_{3(s,298)}$	(5) ΔH_f^0 Nd_2O_3	−1806.9 ± 3. 0[c]
$2La_{(s,298)} + \frac{3}{2}O_{2(g,298)} \rightarrow La_2O_{3(s,298)}$	(6) ΔH_f^0 La_2O_3	−1791.6 ± 1. 0[c]
$2P_{(s,298)} + \frac{5}{2}O_{2(g,298)} \rightarrow P_2O_{5(s,298)}$	(7) ΔH_f^0 P_2O_5	−1504.0 ± 0. 5[d]
$\frac{1}{2}(1-x)La_2O_{3(s,298)} + \frac{1}{2}xNd_2O_{3(s,298)} + \frac{1}{2}P_2O_{5(s,298)} \rightarrow (La_{1-x}Nd_x)PO_4$	(8) $\Delta H_{f,ox}^0$ $(La_{1-x}Nd_x)PO_4$	see Table 2
$\Delta H(8) = -\Delta H(1) + \frac{1-x}{2}\Delta H(2) + \frac{x}{2}\Delta H(3) + \frac{1}{2}\Delta H(4)$		
$(1-x)La_{(s,298)} + xNd_{(s,298)} + P_{(s,298)} + 2O_{2(g,298)} \rightarrow (La_{1-x}Nd_x)PO_4$	(9) $\Delta H_{f,el}^0$ $(La_{1-x}Nd_x)PO_4$	see Table 2
$\Delta H(9) = \frac{x}{2}\Delta H(5) + \frac{1-x}{2}\Delta H(6) + \frac{1}{2}\Delta H(7) + \Delta H(8)$		

Table 2
The enthalpies of drop solution $\Delta H_{ds,973}$ in 3 $Na_2O{\cdot}4\,MoO_3$ at 973 K for $La_{1-x}Nd_xPO_4$ solid solutions with molar fractions $1-x$ of La, the calculated enthalpies of formation from oxides $\Delta H_{f,ox}^0$ at 298 K and from elements $\Delta H_{f,el}^0$ at 298 K using the thermochemical cycle in Table 1, and finally the calculated enthalpy of mixing ΔH_{mix}.

$1-x$	$\Delta H_{ds,973}$(kJ mol^{-1})	$\Delta H_{f,ox}^0$(kJ mol^{-1})	$\Delta H_{f,el}^0$(kJ mol^{-1})	ΔH_{mix}(kJ mol^{-1})
0	145.57 ± 0.21	−309.55 ± 4.26	−1965.9 ± 4.3	0.00 ± 0.14
0.109	147.56 ± 1.61	−314.91 ± 4.55	−1970.4 ± 4.6	−1.37 ± 2.01
0.296	144.89 ± 1.19	−318.01 ± 4.42	−1972.0 ± 4.5	2.36 ± 1.69
0.394	144.58 ± 1.10	−320.72 ± 4.40	−1973.9 ± 4.5	3.23 ± 1.64
0.460	142.78 ± 0.92	−321.76 ± 4.36	−1974.2 ± 4.5	5.41 ± 1.50
0.679	142.30 ± 0.91	−327.22 ± 4.36	−1978.1 ± 4.5	7.13 ± 1.60
0.792	143.70 ± 0.72	−332.13 ± 4.32	−1982.1 ± 4.5	6.38 ± 1.46
0.874	144.53 ± 0.54	−335.48 ± 4.29	−1984.8 ± 4.4	6.01 ± 1.32
1	151.26 ± 0.82	−346.11 ± 4.34	−1994.4 ± 4.5	0.00 ± 0.02

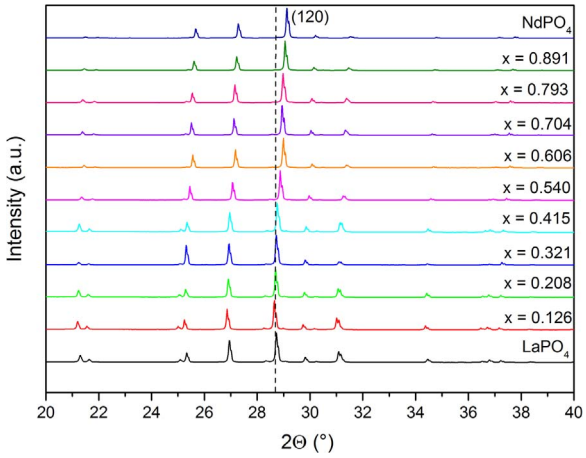

Fig. 1. Selected range of the powder X-ray diffraction patterns of eleven selected compositions (Table 1 of the supplementary information). The first pattern at the bottom belongs to pure $LaPO_4$ and the Nd-content increases from bottom to top (pure $NdPO_4$). The continuous shift of e.g. the (120) reflection is clearly visible (from 28.7° → 29.1°).

repectively. This shift is reasonable, because the ionic radius of Nd^{3+}_{IX} = 1.163 Å is significantly smaller than that of La^{3+}_{IX} = 1.216 Å [15]. As starting structure models for the Rietveld refinements, single crystal data [16] of the pure end-members $LaPO_4$ for the compositional range $x = 0 - 0.49$ and $NdPO_4$ for $x = 0.5 - 1$ were applied. During all refinements La^{3+} and Nd^{3+} shared one identical crystallographic site. Weighted R-values for all refinements were in the range of $R'_{wp} = 2 - 7$ % (background corrected). All values for the goodness-of-fit were in the range of GoF = 1 − 2. An example for the result of a complete Rietveld refinement (1 − x = 0.610; see Table 1 of the Supplementary information) is shown in Fig. 2. The Rietveld model covers the experimental curve almost completely. Very small deviations are visible through the difference curve below. The determined cell constants for all twenty compositions including end-members are shown in Fig. 3. All cell constants a_0, b_0, c_0, the monoclinic angle β (Fig. 3b), as well as the volume of the unit cell V_{uc} show linear relations and obey Vegard's law [17]. They are also consistent to literature values [8]. The calculated densities (Fig. 3c) also show a linear relation. We determined a density of $\rho = 5.06(2)$g/cm^3 for pure $LaPO_4$, which is very similar to the values given by Terra et al. [18] [$\rho = 5.03$ g/cm^3] and Ni et al. [16] [$\rho = 5.08$ g/cm^3], respectively. For pure $NdPO_4$ we obtained $\rho = 5.43(2)$g/cm^3, which is identical to the value given by Ni et al. [16] [$\rho = 5.45$ g/cm^3] for ambient conditions within error limits. The determined cell volumes (Table 1 of the supplementary information) also agree with the systematic trends of the fitted cell volumes of a total of 71 different compositions of synthetic pure and binary monazite-type phases that are plotted as a function of the average cubic radii of the nine-fold coordinated lanthanide cations (Fig. 4). This plot is an extension of the analysis given by [4], and the additional data enable a refinement of their Eq. (1) for the calculation of the unit cell volume as a function of r_k^3:

$$\langle V_{uc}\rangle_w(\text{Å}^3) = (196.020 \pm 0.713) + (61.468 \pm 0.447)\cdot r_K^3(\text{Å}) \quad (1)$$

The correlation coefficient for this fit is $R^2 = 0.99631$ and all data are within a 2σ confidence interval.

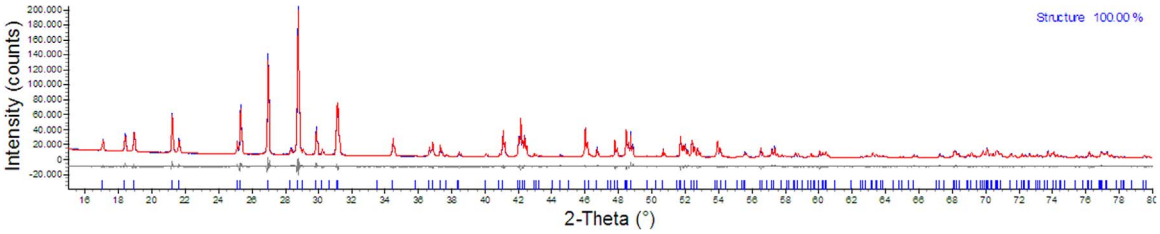

Fig. 2. Complete Rietveld refinement for the composition with $1 - x = 0.610$ (values are given in Table 1 of the Supplementary information). The Rietveld model (red) covers the experimental curve (blue) almost completely. Deviations are visible through the difference curve (grey) below. For a clear illustration, only a section of $2\Theta = 15 - 80°$ has been selected. However, all calculations were carried out for the range $2\Theta = 10 - 130°$. (For interpretation of the references to color in this figure legend, the reader is referred to the web version of this article).

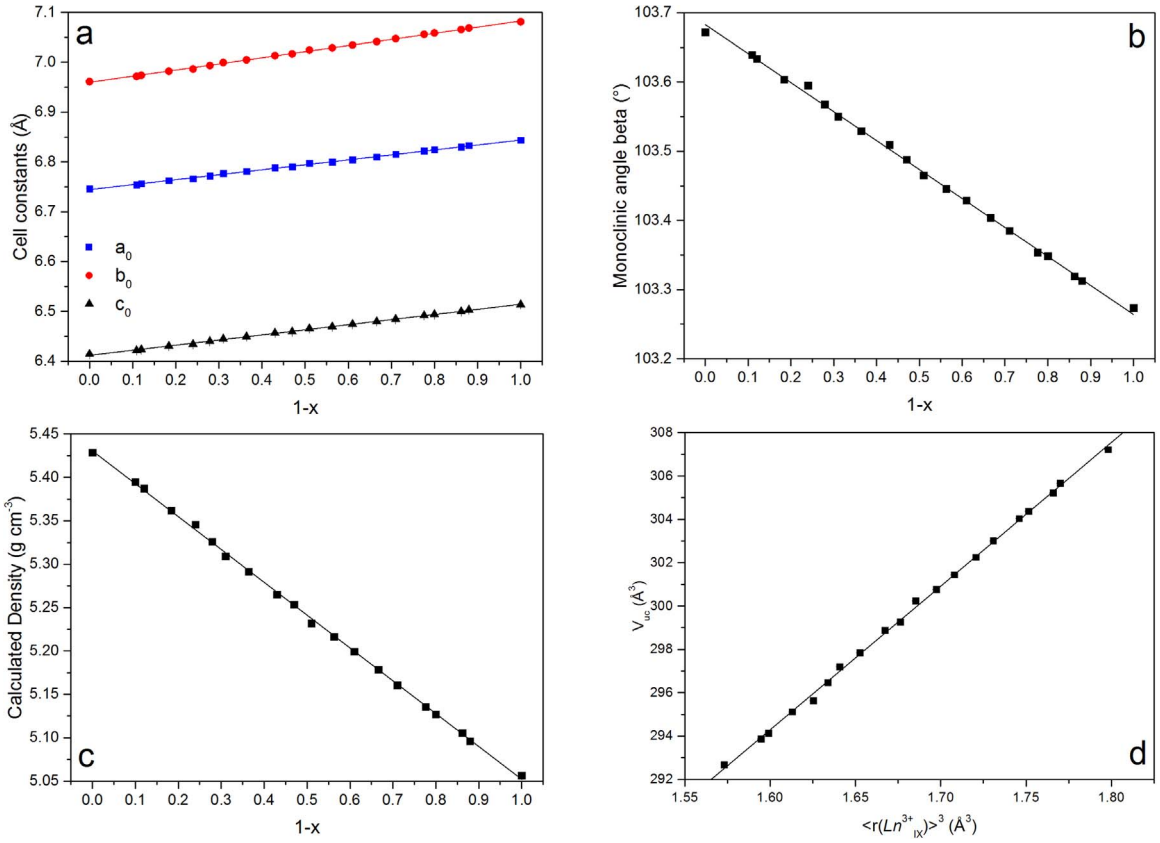

Fig. 3. a) Cell constants a_0 (squares; blue line), b_0 (dots; red line), and c_0 (triangles; bottom line) as a function of composition; b) monoclinic angle β; c) calculated density; d) volume of the unit cell as a function of the average cubic radii $r_K^3(Å^3)$ of the nine-fold lanthanide cations. (For interpretation of the references to color in this figure legend, the reader is referred to the web version of this article).

3.2. Raman and infrared spectroscopy

Eleven out of twenty samples were investigated by infrared spectroscopy (see Table 2 of the Supplementary information). The spectra of the pure end-members and of the mixed phases are very similar (Fig. 5) and compare well to literature data for pure $LaPO_4$ and $NdPO_4$ [21] for all samples and the typical splitting of the $[PO_4]$-bands $\nu_1 \rightarrow \nu_4$ is clearly visible for all compositions. An important result is that no bands that would be typical for pyrophosphates at wavenumbers $\approx 870 - 1260\ cm^{-1}$ or metaphosphates $\approx 600 - 900\ cm^{-1}$ are visible within the spectral range [21].

Raman spectroscopy provides more specific information about the influence of composition on short-range order. Fig. 6 shows the shift of the two $[PO_4]$ stretching vibrations (ν_1: symmetric stretch and ν_3: anti-symmetric stretch) to larger wavenumbers with increasing Nd-content. The decreasing average cation radius simultaneously causes decreasing (P – O) bond lengths. Consequently the frequencies of the stretching vibrations will be increased, an observation that has already been extensively investigated and described by Popović et al. [22], and is interpreted as a common response of phosphate crystal structures. The frequencies of the determined $[PO_4]$ bands for the pure end-members given in Fig. 7, agree with literature data [23–25] and all four modes for all compositions exhibit strong linear relations with composition, which probably would not be present if chemical inhomogeneities would be a dominant structural feature.

However, with increasing Nd content, the symmetric $[PO_4]$ stretching band ν_1 at $967\ cm^{-1}$ (pure $LaPO_4$) broadens and shifts towards larger wavenumbers (Fig. 8), reflecting slight structural changes. The band broadening reflects the general decrease of the lifetime of phonons [26]. The observed shift towards larger wavenumbers indicates a moderate shortening of P – O bonds [22] caused by distortion and tilting of the $[PO_4]$ tetrahedra. The full width at half maximum (FWHM) determined for pure $LaPO_4$ is $2.88 \pm 0.08\ cm^{-1}$, and this value increases up to $3.27 \pm 0.02\ cm^{-1}$ (Fig. 9). Some of the observed changes of the FWHM may result from differences in sample preparation but the main cause probably reflects structural differences. A similar broadening of

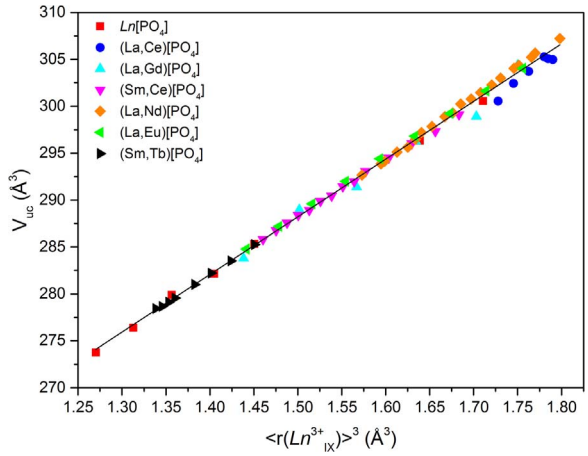

Fig. 4. Linear fit of the average cubic radii r_K^3(Å^3) of the nine-fold lanthanide cations [15] in pure monoclinic orthophosphates and in well characterized solid solutions versus the weighted mean values of the corresponding unit cell volumes V_{uc}(Å^3). Error bars are within symbol size. 71 different compositions were included in the linear fit ($R^2 = 0.99631$). The result of this fit is expressed by Eq. (1). The data for LnPO$_4$, (La, Ce)PO$_4$, (La, Gd)PO$_4$ and (Sm, Ce)PO$_4$, respectively, are identical to that used in [4]. The data for (La, Nd)PO$_4$ can be found in Table 1 of the Supplementary information. (La, Eu)PO$_4$ is from [19], and (Sm, Tb)PO$_4$ from [20].

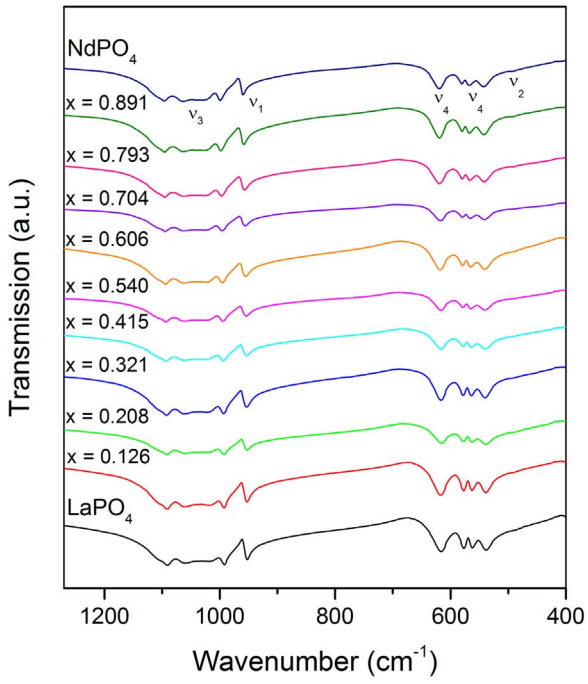

Fig. 5. Normalized IR spectra of all eleven compositions listed in Table 2 of the Supplementary information, in the range of 400 – 1250 cm^{-1}. The first spectrum at the bottom belongs to pure LaPO$_4$ and the Nd-content increases from bottom to top (pure NdPO$_4$). The typical splitting of the [PO$_4$]-bands $\nu_1 \rightarrow \nu_4$ is clearly visible for all compositions. No bands that would be typical for pyrophosphates at wavenumbers ≈ 870 – 1260 cm^{-1} or metaphosphates ≈ 600 – 900 cm^{-1}, respectively, are visible within the spectral range [21].

ν_1 and a similar shift towards larger wavenumbers has been observed for pure CePO$_4$ as a function of pressure [27]. With increasing pressure the Ce – O bond length and the P – O bond length both decrease, and the same happens in La$_{1-x}$Nd$_x$PO$_4$ solid solutions with increasing Nd content. The average Ln – O bond length (Ln = La, Nd) and the average P – O bond length also both decrease significantly, as does the volume of the unit cell. In pure LaPO$_4$ the average La – O bond length is 2.5785 Å and the average P – O bond length is 1.5384 Å [16]. In pure NdPO$_4$ these values are significantly smaller: Nd – O = 2.5245 Å and P – O = 1.5366 Å. Therefore, because of the different radii of La^{3+} and Nd^{3+}, in solid solutions the atomic positions of the cations are slightly shifted from the ideal positions. A similar observation was made for cheralite CaTh(PO$_4$)$_2$ [28], which also has a monazite-type crystal structure, at ambient conditions.

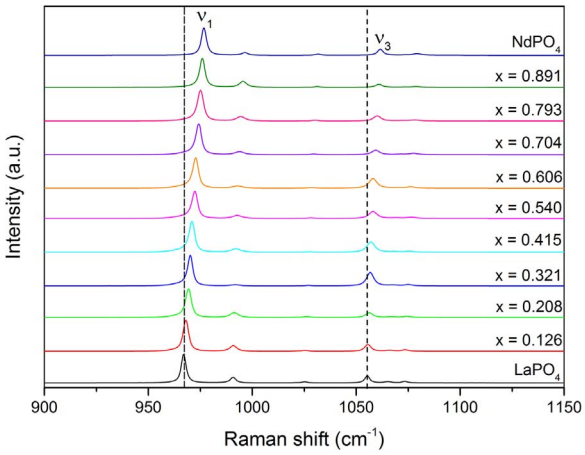

Fig. 6. Selected range of unpolarized Raman spectra of eleven compositions (Table 2 of the Supplementary information) that show a continuous shift to larger wavenumbers of the symmetric (ν_1) and the anti-symmetric (ν_3) stretching vibration of the [PO$_4$] tetrahedra with increasing Nd-content. The first spectrum at the bottom belongs to pure LaPO$_4$ and the Nd-content increases from bottom to top (pure NdPO$_4$).

3.3. High temperature calorimetry

The analytical methods we have applied yielded no indications for phase separation or chemical inhomogeneities. Therefore a homogeneous average longe-range distribution of cations can be anticipated, although there is indication of moderate changes of short-range order as discussed above. Using high temperature oxide melt solution calorimetry we determined the enthalpy of drop solution $\Delta H_{ds,973}$ for the solid solutions (see Section 2.3), and these values, together with an appropiate thermochemical cycle, enabled us to calculate the enthalpy of formation from the oxides $\Delta H^0_{f,ox}$ and from the elements $\Delta H^0_{f,el}$, respectively (Table 2), and finally the enthalpy of mixing ΔH_{mix} (last column in Table 2). However, the $\Delta H_{ds,973}$ value for LaPO$_4$ published by Ushakov et al. [14] is out of range, but fortunately we had the chance to re-measure the original samples of Ushakov et al. [14] under improved experimental conditions (see Section 2.3). During the experiments of Ushakov et al. [14] accidently no gas bubbling occurred in the calorimeter (pers. comm. with S. Ushakov). This is the only difference to our repeated experiments. We measured the same samples and we even used the identical calorimeter. In order to assure, that we did not measure hydrated samples, all samples were dried at T = 1073 K for about 12 h before the measurements. The new values of the repeated measurement of the Ushakov material, the material of this work, as well as the LaPO$_4$ endmembers of Hirsch et al. [46] and Neumeier et al. (2017; measured during the same campaign) were in very good agreement. As a result the old data point for pure LaPO$_4$ determined by Ushakov et al. ($\Delta H_{ds,973} = 143.73 \pm 0.89\ kJ/mol$) was totally out of range in Fig. 10. Because new data for most of the remaining pure phase (TbPO$_4$, GdPO$_4$, EuPO$_4$ and SmPO$_4$) are available, we are quite sure that the new data point for LaPO$_4$ is reliable. Additionally recent data given by Janots et al. [29] were included and all data together allow the calculation of reasonable values of $\Delta H^0_{f,ox}$ for pure LaPO$_4$. Fig. 10 shows the strong linear relation between the ionic radii of the lanthanide cations (3+, 9-fold coordination [15]) and the enthalpy of drop solution $\Delta H_{ds,973}$ for the pure end members. This linear trend supports the accuracy of $\Delta H_{ds,973}$ values used in our calculations of the two end members LaPO$_4$ and NdPO$_4$. Recently Rawat et al. [33] published new high temperature calorimetric data for LaPO$_4$. They determined sig-

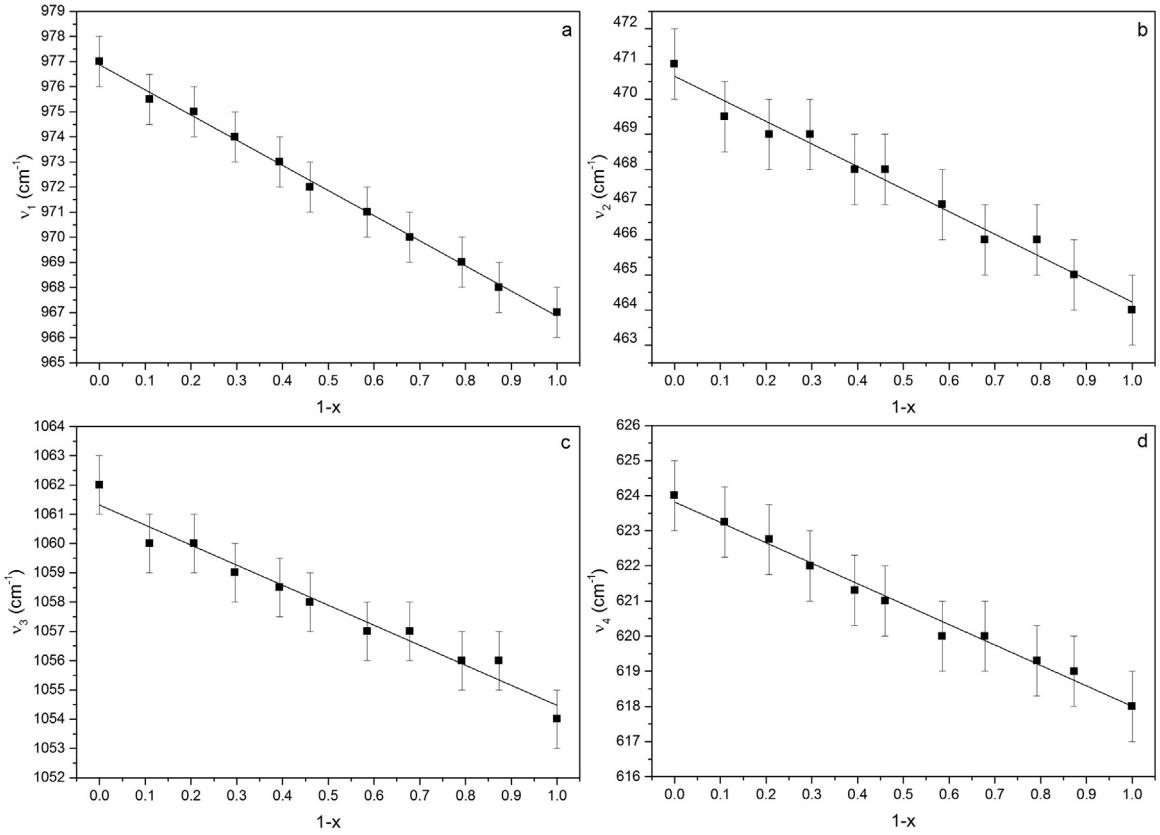

Fig. 7. Linear fits of the mean [PO_4] normal modes ν_i(cm^{-1}) vs. mole fraction 1 − x of $LaPO_4$. a) ν_1 – symmetric stretch; b) ν_2 – symmetric bending; c) ν_3 – anti-symmetric stretch; d) ν_4 – anti-symmetric bending.

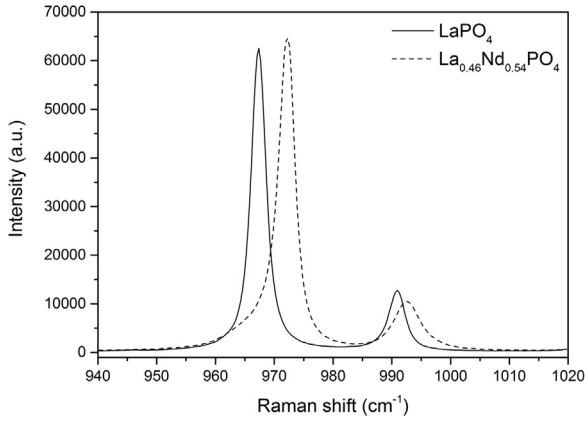

Fig. 8. Comparison of the symmetric Raman stretching band ν_1 (left) for pure $LaPO_4$ (solid curve) and $La_{0.46}Nd_{0.54}PO_4$ (dashed curve), respectively. This figure shows the shift to a larger wave number, the increase of the FWHM, and increasing development of band asymmetry with increasing Nd content of the solid solution. The two latter spectral changes strongly suggest a change in short-range order.

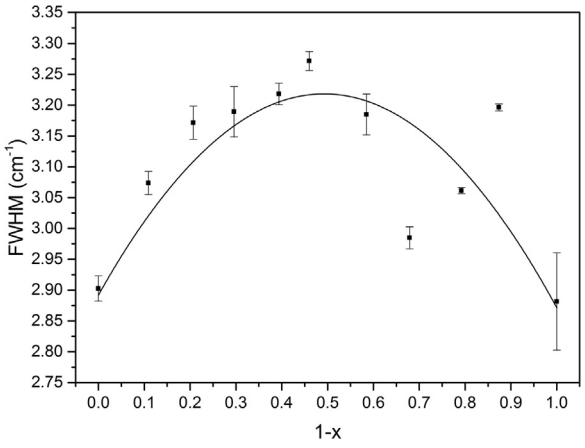

Fig. 9. Development of the FWHM of the symmetric Raman stretching band ν_1 as a function of composition. The data represent average values of four or five measurements per composition and the error bars represent the uncertainties of the calculated mean values. The data were fitted using a second degree polynomial (R^2 = 0.99951).

nificantly lower values for $\Delta H^0_{f,ox}$ and $\Delta H^0_{f,el}$, respectively, compared to our results (Table 2). Even the heat capacities they determined differ significantly to established reference data (see e.g. Kowalski et al. [34] and references therein). The data of [33] were not taken into account for our own calculations.

Fig. 11 shows the calculated enthalpy of mixing as a function of composition. Squares denote the experimental data and the solid line represents the best fit to this data, using a third degree polynomial. The asymmetry of ΔH_{mix} is clearly visible and ΔH_{mix} shows a maximum at x = 0.299 (ΔH_{mix} = 7.53 ± 0.01 kJ mol^{-1}). We used the Redlich-Kister equation [30,31] for the calculation of two Margules interaction parameters from ΔH_{mix} of this subregular binary solution [32]:

$$\frac{\Delta H_{mix}}{x(1-x)} = W_1 + (W_2 - W_1)\cdot x \quad (2)$$

This linear equation enables the determination of W_1 as the intercept and (W_2 − W_1) as the slope of a straight line derived by linear least squares fitting of the data points. Taking an average error of ±0.004 for all compositions into account (see Section 2.2) and the error of ΔH_{mix} as given in Table 2, one gets the following fit-parameters: W_1 = 60.50 ± 4.02 kJ mol^{-1} and W_2 = − 17.52 ± 11.35 kJ mol^{-1} (R^2 = 0.94934).

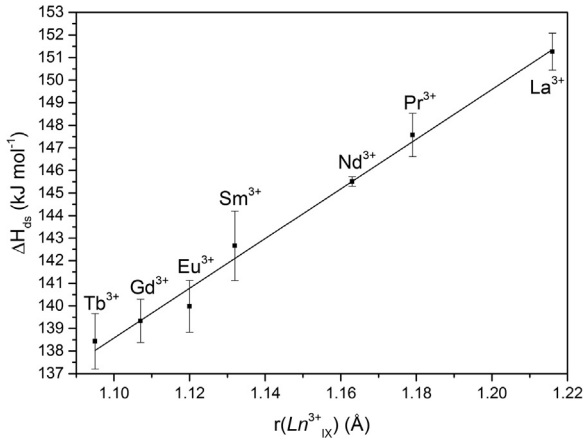

Fig. 10. Linear regression of the enthalpy of drop solution at 973 K for pure $Ln PO_4$ end members. Values for $LaPO_4$ and $NdPO_4$ are given in Table 2 of the supplementary information. Values for $PrPO_4$ are taken from [46], values for $SmPO_4$ and $TbPO_4$ are from [14], and finally values for $EuPO_4$ and $GdPO_4$ were taken from [45].

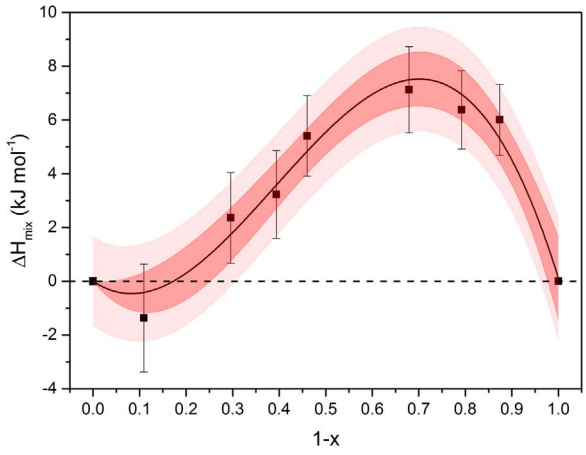

Fig. 11. Enthalpy of mixing as a function of composition. Experimental values are given in Table 2 of the supplementary information. The red area shows the 95% confidence interval and the light red area shows the 95% prediction band, respectively.

3.4. Joint analysis of structural and thermodynamic properties

The enthalpies of mixing are in the expected range for a solid solution in which phase separation or compound formation is not observed. Similar results were e.g. obtained for comparable phases like the endothermic eastonite-phlogopite mica system, with $\Delta H_{mix} \leq 12.57$ kJ mol^{-1} [36], and for the exothermic spinel system $Fe_3O_4 - Fe_{8/3}O_4$, with $\Delta H_{mix} \geq -10.84$ kJ mol^{-1} [32]. The subregular model is the simplest model for asymmetric solutions, and has been widely used in the mineralogical literature. It represents an extension of the regular solution model by making the Margules interaction parameter W a simple function of composition ($W = W_1X_2 + W_2X_1$). Therefore, the subregular model is a weighted average of two regular solution models fitted to the data near the two terminal segments of a binary solution (see e.g. [37], chp. 9.2, p. 256–273). In other words, the symmetric Margules formulation is just a special case of the more general approach, that also takes short-range order into account (see [38] for a comprehensive explanation). Here, short-range order simply means the average regular environment of a cation within short distances (e.g. ≤5 Å), characterized by interatomic distances or bond lengths, bond angles, and coordination numbers. The loss in short-range order can be quantified quite easily, by the structural analysis of the $[PO_4]$-tetrahedra and the $[LnO_4]$-polyhedra and their respective environments. Using the structural data published by Ni et al. [16] (see also Section 3.2), the average P-O bond length is equal 1.5384 Å for $LaPO_4$ and 1.5366 Å for $NdPO_4$ (- 0.12%), respectively. The average LnO bond length decreases from 2.5785 Å ($LaPO_4$) down to 2.5245 Å ($NdPO_4$), that represents a reduction of about 2.1%. In the crystal structure of $NdPO_4$ the $[PO_4]$-tetrahedra are significantly smaller and more regular than they are in the structure of $LaPO_4$, i.e. the variation of bond lengths is less pronounced. However, the $[LnO_4]$-polyhedra are even smaller, but less regular in $NdPO_4$ compared to $LaPO_4$. As a consequence the phosphorus environment of the La^{3+} cation is more regular in $LaPO_4$ than that of Nd^{3+} in $NdPO_4$. The opposite is true for the P-P environment. This is significantly more regular in the structure of $NdPO_4$ compared to $LaPO_4$. Fig. 12 is an illustrating example of inevitably occurring polyhedral distortions, by visualizing different Ln-O-P bond angles in $LaPO_4$ (left) and $NdPO_4$ (right), respectively. With an increasing amount of $NdPO_4$ in the structure of $LaPO_4$, the $[LnO_4]$-polyhedra will be clearly changed to a greater extent than the $[PO_4]$-tetrahedra. This result is consistent with the findings of Huittinen et al. [39], who probed the structural homogeneity of Eu^{3+}-doped $La_{1-x}Gd_xPO_4$ monazite-type solid solutions by a combinatorial approach using Raman spectroscopy, time-resolved laser fluorescence spectroscopy (TRLFS), and computer simulations. They also concluded, that increasing amounts of $GdPO_4$ mixed with $LaPO_4$ result in a loss of short-range order, showing a stronger distortion around the lanthanide cation site than around the phosphate anion (see also [40,41] for recent reviews on the correlation of local structure and the thermochemistry of phosphate solid solutions). However, the system $LaPO_4 - GdPO_4$ is assumed to be a symmetrical regular solution [45], and not a subregular one.

Currently our results can be interpreted as follows: The symmetry

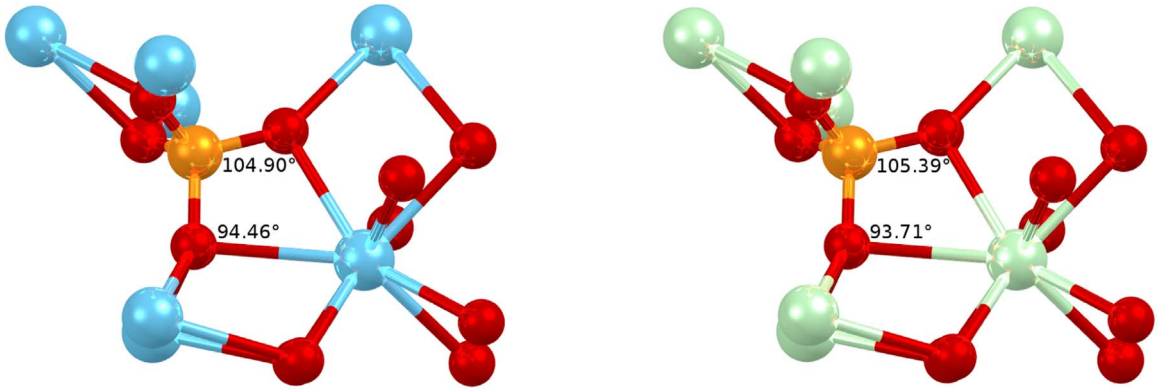

Fig. 12. Detail of the monazite crystal structure: $LaPO_4$ (left) and $NdPO_4$ (right) with an arbitrary, but identical viewing direction (P - orange, O - red, La - blue, Nd - green). Both fragments appear similar, but bond lengths and bond angles differ significantly (see text). The La-O-P bond angle is 104.90° and 94.46° within the molecule on the left hand side, and the Nd-O-P bond angle is equal 105.39° and 93.71° on the right hand side of this graph. (For interpretation of the references to color in this figure legend, the reader is referred to the web version of this article).

of the FWHM as a function of composition (Fig. 9) elucidates, that from a structural point of view it is not crucial from which side of the system one starts to incorporate additional cations into the structure. Starting from pure $NdPO_4$ (left hand side of Fig. 9) the effort for the incorporation of larger lanthanum cations appears quite the same as vice versa. But even though the overall structure remains constant, short-range order changes can be detected by a clearly visible increase of the FWHM. However, differences are still rather small, with a maximum $\Delta FWHM \approx 0.33\ cm^{-1}$, and the increase in FWHM at intermediate compositions is consistent with a larger variety of local environments, which would exist even with a close to random arrangement of cations. This is generally expected in a solid solution.

The enthalpies of formation that are listed in Table 2 prove that $LaPO_4$ is more stable with respect to the binary oxides than to $NdPO_4$. $\Delta H^0_{f,ox}$ is about $37 kJ \cdot mol^{-1}$ more negative for pure $LaPO_4$.

In summary, $La_{1-x}Nd_xPO_4$ monazite-type solid solutions show a change of short-range order and an asymmetrical development of the enthalpy of mixing ΔH_{mix} with increasing Nd content. Therefore, this system behaves differently from comparable systems like $La_{1-x}Gd_xPO_4$ and $La_{1-x}Eu_xPO_4$ [45], respectively, but even the system $La_{1-x}Pr_xPO_4$ [46] shows a non-symmetrical development of ΔH_{mix}. It must therefore be emphasized that a symmetrical development of ΔH_{mix} as a function of composition can not be easily assumed for all $La_{1-x}Ln_xPO_4$ solid solutions (*Ln*=Ce, Pr, Nd, Pm, Sm, Eu, Gd). Before our measurements, the asymmetric behaviour of the enthalpy of mixing has not been detected. We used Nd as a surrogate for Am. A smaller value for the enthalpy of mixing means a more stable solid solution, which is an essential property of a ceramic nuclear waste form. Therefore, according to Fig. 11, only smaller amounts of Am should be added to $LaPO_4$, in order to keep the enthalpy of mixing reasonably small. However, all these results together indicate, that rare earth cation radius probably is the dominant controlling factor.

4. Conclusions

All analytical results suggest that $La_{1-x}Nd_xPO_4$ is a homogeneous solid solution without any phase separation, domain building, or tendency toward compound formation. Therefore our results support the conclusions given by Maron et al. [8] that this solid solution is a single phase and that sample preparation and processing are crucial for sample quality. All cell constants, the volume of the unit cell, the density, and even the vibrational modes show strong linear relations with composition. The determined unit cell volumes of all twenty compositions investigated within this work, fit trends seen in other lanthanide monazite-type phases, regardless of whether one or two lanthanide cations are present on the nine-fold coordinated sites. However, the results of our Raman measurements clearly show structural changes as a function of composition in the solid solution. Increased FWHM and increasing development of band asymmetries are consistent with possible bond length changes and greater variability in local Ln–O and P–O environment. High temperature oxide melt solution calorimetric experiments indicate a subregular (asymmetric) solid solution. The enthalpies of mixing are consistent with a homogeneous solid solution without phase separation above ambient temperature.

Acknowledgements

This work was supported by the German Research Association (Deutsche Forschungsgemeinschaft DFG; Project-No. SCHL495/3-1). The financial support is gratefully acknowledged. Special thanks go to H. Curtius and Z. Paparigas for the support of the IR measurements, to A. Bukaemskiy for supporting the pellet preparation, and to P. Kowalski and V. Vinograd for very fruitful discussions (all Forschungszentrum Jülich, IEK-6). The calorimetric studies were supported as part of the Materials Science of Actinides, an Energy Frontier Research Center funded by the U.S. Department of Energy, Office of Science, Office of Basic Energy Sciences [Grant DESC0001089].

Appendix A. Supplementary data

Supplementary data associated with this article can be found in the online version at http://dx.doi.org/10.1016/j.jssc.2018.11.040.

References

[1] W.J. Weber, A. Navrotsky, S. Stefanovsky, E.R. Vance, E. Vernaz, Materials science of high-level nuclear waste immobilization, MRS Bull. 34 (2009) 46–53.
[2] N. Clavier, R. Podor, N. Dacheux, Crystal chemistry of the monazite structure, J. Eur. Ceram. Soc. 31 (2011) 941–976.
[3] N. Dacheux, N. Clavier, R. Podor, Monazite es a promising long-term radioactive waste matrix: benefits of high-structural flexibility and chemical durability, Am. Mineral. 98 (2013) 833–847.
[4] H. Schlenz, J. Heuser, A. Neumann, S. Schmitz, D. Bosbach, Monazite as a suitable actinide waste form, Z. Krist. 228 (2013) 113–123.
[5] F. Brandt, S. Neumeier, T. Schuppik, Y. Arinicheva, A. Bukaemskiy, G. Modolo, D. Bosbach, Conditioning of minor actinides in lanthanum monazite ceramics: a surrogate study with Europium, Prog. Nucl. Energy 72 (2014) 140–143.
[6] G.R. Lumpkin, Ceramic waste forms for actinides, Elements 2 (2006) 365–372.
[7] A.C. Palke, J.F. Stebbins, Paramagnetic interactions in the ^{31}P NMR spectroscopy of rare earth element orthophosphate ($REPO_4$, monazite/xenotime) solid solutions, Am. Mineral. 96 (2011) 1343–1353.
[8] S. Maron, G. Dantelle, T. Gacoin, F. Devreux, NMR and ESR relaxation in Nd- and Gd-doped $LaPO_4$: towards the accurate determination of the doping concentration, Phys. Chem. Chem. Phys. 16 (2014) 18788–18798.
[9] K. Popa, R.J.M. Konings, T. Geisler, High temperature calorimetry of $(La_{1-x}Ln_x)PO_4$ solid solutions, J. Chem. Thermodyn. 39 (2007) 236–239.
[10] Y. Li, P.M. Kowalski, A. Blanca-Romero, V. Vinograd, D. Bosbach, Ab initio calculation of excess properties of $La_{1-x}(Ln, An)_xPO_4$ solid solutions, J. Solid State Chem. 220 (2014) 137–141.
[11] A. Navrotsky, Progress and new directions in calorimetry: a 2014 perspective, J. Am. Ceram. Soc. 97 (2014) 3349–3359.
[12] A. Navrotsky, Progress and new directions in high temperature calorimetry, Phys. Chem. Miner. 2 (1977) 89–104.
[13] A. Navrotsky, Progress and new directions in high temperature calorimetry revisited, Phys. Chem. Miner. 24 (1997) 222–241.
[14] S.V. Ushakov, K.B. Helean, A. Navrotsky, Thermochemistry of rare-earth orthophosphates, J. Mater. Res. 16 (2001) 2623–2633.
[15] R.D. Shannon, Revised effective ionic radii and systematic studies of interatomic distances in halides and chalcogenides, Acta Cryst. A32 (1976) 751–767.
[16] Y. Ni, J.M. Hughes, A.N. Mariano, Crystal chemistry of the monazite and xenotime structures, Am. Mineral. 80 (1995) 21–26.
[17] L. Vegard, Die Konstitution der Mischkristalle und die Raumfüllung der Atome, Z. für Phys. 5 (1921) 17–26.
[18] O. Terra, N. Clavier, N. Dacheux, R. Podor, Prepraration and characterization of lanthanum-gadolinium monazites as ceramics for radioactive waste storage, New J. Chem. 27 (2003) 957–967.
[19] Y. Arinicheva, A. Bukaemskiy, S. Neumeier, G. Modolo, D. Bosbach, Studies on thermal and mechanical properties of monazite-type ceramics for the conditioning of minor actinides, Prog. Nucl. Energy 72 (2014) 144–148.
[20] J. Heuser, Monazite-type ceramics as potential waste forms for the disposal of minor actinides and Pu, PhD-thesis, Schriften des Forschungszentrums Jülich (german), Reihe Energie und Umwelt / energy and environment 278, ISBN 978-3-95806-076-0, 2015.
[21] J. Heuser, A.A. Bukaemskiy, S. Neumeier, A. Neumann, D. Bosbach, Raman and infrared spectroscopy of monazite-type ceramics used for nuclear waste conditioning, Prog. Nucl. Energy 72 (2014) 149–155.
[22] L. Popović, D. de Waal, J.C.A. Boeyens, Correlation between Raman wavenumbers and P -O bond lengths in crystalline inorganic phosphates, J. Raman Spectrosc. 36 (2005) 2–11.
[23] G.M. Begun, G.W. Beall, L.A. Boatner, W.J. Gregor, Raman Spectra of the rare earth orthophosphates, J. Raman Spectrosc. 11 (1981) 273–278.
[24] R. Podor, Raman spectra of the actinide-bearing monazites, Eur. J. Mineral. 7 (1995) 1353–1360.
[25] E.N. Silva, A.P. Ayala, I. Guedes, C.W.A. Paschoal, R.L. Moreira, C.-K. Loong, L.A. Boatner, Vibrational spectra of monazite-type rare-earth orthophosphates, Opt. Mater. 29 (2006) 224–230.
[26] L. Nasdala, R. Grötzschel, S. Probst, B. Bleisteiner, Irradiation damage in Monazite-(Ce): an example to establish the limits of Raman confocality and depth resolution, Can. Mineral. 48 (2010) 351–359.
[27] T. Huang, J.-S. Lee, J. Kung, C.-M. Lin, Study of monazite under high pressure, Solid State Commun. 150 (2010) 1845–1850.
[28] P.E. Raison, S. Heathman, G. Wallez, C.E. Zvoriste, D. Bykov, G. Menard, E. Suard, K. Popa, N. Dacheux, R.J.M. Konings, R. Caciuffo, Structure and nuclear density distribution in the cheralite - $CaTh(PO_4)_2$: studies of its behaviour under high pressure (36 GPa), Phys. Chem. Miner. 39 (2012) 685–692.
[29] E. Janots, F. Brunet, B. Goffé, C. Poinssot, M. Burchard, L. Cemič,

Thermochemistry of monazite-(La) and dissakisite-(La): implications for monazite and allanite stability in metapelites, Contrib. Mineral. Petrol. 154 (2007) 1–14.
[30] O. Redlich, A.T. Kister, Thermodynamics of nonelectrolyte solutions - X-y-t relations in a binary system, Ind. Eng. Chem. 40 (1948) 341–345.
[31] O. Redlich, A.T. Kister, Thermodynamics of nonelectrolyte solutions - algebraic representation of thermodynamic properties and classification of solutions, Ind. Eng. Chem. 40 (1948) 345–348.
[32] K.I. Lilova, F. Xu, K.M. Rosso, C.I. Pearce, S. Kamali, A. Navrotsky, Oxide melt solution calorimetry of Fe^{2+}-bearing oxides and application to the magnetite-maghemite (Fe_3O_4 – $Fe_{8/3}O_4$) system, Am. Mineral. 97 (2012) 164–175.
[33] D. Rawat, S. Phapale, R. Mishra, S. Dash, Thermodynamic studies on charge-coupled substituted synthetic monazite, J. Nucl. Mater. 487 (2017) 406–417.
[34] P.M. Kowalski, G. Beridze, V.L. Vinograd, D. Bosbach, Heat capacities of lanthanide and actinide monazite-type ceramics, J. Nucl. Mater. 464 (2015) 147–154.
[35] E.I. Get'man, S.V. Radio, Mixing energies (Interaction Parameters) and decomposition temperatures in solid solutions of monazites of rare earth elements with structure $La_{1-x}Ln_xPO_4$, Inorg. Mater. 53 (2017) 718–721.
[36] S. Circone, A. Navrotsky, Substitution of $^{[6,4]}$Al in phlogopite: high temperature solution calorimetry, heat capacities, and thermodynamic properties of the phlogopite-eastonite join, Am. Mineral. 77 (1992) 1191–1205.
[37] J. Ganguly, Thermodynamic solution and mixing models: non-electrolytes, in: J. Ganguly (Ed.)Thermodynamics in Earth and Planetary Sciences, Springer-Verlag Berlin Heidelberg, Germany, 2008, pp. 249–279.
[38] V. Vinograd, Configurational entropy of binary silicate solid solutions, in: C. Geiger (Ed.), EMU Notes in Mineralogy, Eötvös University Press, Budapest, 2001, pp. 303–346.
[39] N. Huittinen, Y. Arinicheva, P.M. Kowalski, V.L. Vinograd, S. Neumeier, D. Bosbach, Probing structural homogeneity of $La_{1-x}Gd_xPO_4$ monazite-type solid solutions by combined spectroscopic and computational studies, J. Nucl. Mater. 486 (2017) 148–157.
[40] H. Schlenz, S. Neumeier, A. Hirsch, L. Peters, G. Roth, Phosphates as safe containers for radionuclides, in: S. Heuss-Aßbichler, G. Amthauer, M. John (Eds.), Highlights in Applied Mineralogy, De Gruyter Berlin Boston, 2017, pp. 171–195.
[41] S. Neumeier, Y. Arinicheva, Y. Ji, J. Heuser, P. Kowalski, P. Kegler, H. Schlenz, D. Bosbach, G. Deissmann, New insights into phosphate based materials for the immobilisation of actinides, Radiochim. Acta 105 (2017) 961–985.
[42] J.H. Cheng, A. Navrotsky, Enthalpies of formation of $LaBO_3$ perovskites (B = Al, Ga, Sc, and In), J. Mater. Res. 18 (2003) 2501–2508.
[43] A. Navrotsky, W. Lee, A. Mielewczyk-Gryn, S.V. Ushakov, A. Anderko, H. Wu, R.E. Riman, Thermodynamics of solid phases containing rare earth oxides, J. Chem. Thermodyn. 88 (2015) 126–141.
[44] R.A. Robie, B.S. Hemingway, Thermodynamic properties of minerals and related substances at 298.15 K and 1 Bar (10^5 Pascals) pressure and at higher temperatures, U.S. Geol. Surv. Bull. 2131 (1979) (Washington, DC).
[45] S. Neumeier, P. Kegler, Y. Arinicheva, A. Shelyug, P. Kowalski, C. Schreinemachers, A. Navrotsky, D. Bosbach, Thermochemistry of $La_{1-x}Ln_xPO_4$-monazites (Ln = Gd, Eu), J. Chem. Thermodyn. 105 (2017) 396–403.
[46] A. Hirsch, P. Kegler, I. Alencar, J. Ruiz-Fuertes, A. Shelyug, L. Peters, C. Schreinemachers, A. Neumann, S. Neumeier, H.-P. Liermann, A. Navrotsky, G. Roth, Structural, vibrational, and thermochemical properties of the monazite-type solid solution $(La_{1-x}Pr_x)PO_4$, J. Solid State Chem. 245 (2017) 82–88.